

Three-dimensional lattice Boltzmann flux solver for simulation of fluid-solid conjugate heat transfer problems with curved boundary

L. M. Yang ¹, C. Shu,^{1,*} Z. Chen,¹ and J. Wu²

¹*Department of Mechanical Engineering, National University of Singapore, 10 Kent Ridge Crescent, 119260 Singapore*

²*Department of Aerodynamics, College of Aerospace Engineering, Nanjing University of Aeronautics and Astronautics, Yudao Street, Nanjing 210016, Jiangsu, China*



(Received 2 December 2019; revised manuscript received 12 April 2020; accepted 5 May 2020; published 21 May 2020)

A three-dimensional (3D) lattice Boltzmann flux solver is presented in this work for simulation of fluid-solid conjugate heat transfer problems with a curved boundary. In this scheme, the macroscopic governing equations for mass, momentum, and energy conservation are discretized by the finite-volume method, and the numerical fluxes at the cell interface are reconstructed by the local solution of lattice Boltzmann equation. For solving the 3D fluid-solid conjugate heat transfer problems, the density distribution function (D3Q15 model) is utilized to compute the numerical fluxes of continuity and momentum equations, and the total enthalpy distribution function (D3Q7 model) is introduced to calculate the numerical flux of the energy equation. The connections between the macroscopic fluxes and the local solution of the lattice Boltzmann equation are provided by the Chapman-Enskog expansion analysis. As compared with the lattice Boltzmann method, in which the time step and grid spacing are correlated, the local solution of the lattice Boltzmann equation at each cell interface used in the present scheme is independent of each other. As a result, the drawback of the tie-up between the time step and grid spacing can be effectively removed and the developed method applies very well to nonuniform mesh and curved boundaries. To validate the performance of the developed method, the steady and unsteady natural convection in a finned 3D cavity and in a finned 3D annulus are simulated. Numerical results showed that the present scheme can effectively solve the 3D conjugate heat transfer problems with a curved boundary.

DOI: [10.1103/PhysRevE.101.053309](https://doi.org/10.1103/PhysRevE.101.053309)

I. INTRODUCTION

Heat transfer between different components is one of the fundamental issues in multiphase/multicomponent systems. It has numerous applications in many areas, such as in electronic cooling devices [1–3], thermal design of buildings [4–6], crystal growth [7,8], and solar collectors [9,10]. In these flow problems, the thermophysical properties can change sharply between different components such as solid and fluid, or different solid media. Furthermore, the fluid flow and heat transfer are coupled in the fluid-solid conjugate heat transfer problems. These features increase the difficulty of numerical simulation, especially for three-dimensional (3D) fluid-solid conjugate heat transfer problems with complicated geometry.

As a new numerical approach, the lattice Boltzmann method (LBM) [11–14] has drawn increasing attention for its simplicity and been widely applied to simulate heat and mass transfer between multiphases or different materials. Aiming to solve the steady-state conjugate heat transfer problems, a half-lattice division LBM was proposed by Wang *et al.* [15]. In their method, the continuity conditions of both temperature and heat flux are satisfied automatically by placing the conjugate interface in the middle of two lattice nodes which are located in different components. This method has been suc-

cessfully applied to predict the effective thermal conductivity of various porous [16] and simulated heat transfer between two flows at different temperatures separated by a solid wall with finite thickness [17]. Meng *et al.* [18] developed an on-node LBM, in which the conjugate interface is located exactly on the lattice nodes, for simulation of both steady and transient conjugate heat transfer problems. In this scheme, the continuity conditions of temperature and heat flux are imposed by modifying the distribution functions around the conjugate interface. Imani *et al.* [19] have successfully applied this scheme to simulate multiple heated obstacles mounted in a channel. However, it should be pointed out that the above two schemes are limited to straight-interface geometry. To simulate conjugate heat transfer problems with a curved boundary, a general interface scheme was proposed by Li *et al.* [20] and further extended to the discontinuity conjugated interfacial conditions by Guo *et al.* [21], Hu *et al.* [22], and Mu *et al.* [23]. Similar to the work of Meng *et al.* [18], the essential idea of the general interface scheme is to satisfy the conjugate conditions by establishing an analytical relationship for the distribution functions around the conjugate interface. In addition, Karani and Huber [24], Rihab *et al.* [25], and Chen *et al.* [26] simulated the conjugate heat transfer problems by applying the thermal lattice Boltzmann equation with an additional source term. Very recently, Nouri *et al.* [27] further extended the method of Rihab *et al.* [25] to simulate the 3D conjugate heat transfer problems in heterogeneous media.

*Corresponding author: mpeshuc@nus.edu.sg

In the above LBM, the conventional lattice Boltzmann models for thermal flow, such as the model of energy [28] and the model of temperature [29], can be applied directly to solve the conjugate heat transfer problems. A comprehensive review of the thermal LBM can be found in the work of Li *et al.* [30]. However, a specific treatment of the distribution functions around the conjugate interface or an additional source term is required, which complicates the implementation of LBM. To keep the inherent simplicity of the standard LBM, considerable efforts have been devoted to modifying the thermal lattice Boltzmann models. By introducing a reference specific heat to decouple the specific heat and the thermal conductivity, Huang and Wu [31] proposed a D2Q9 model of total enthalpy. Subsequently, a D2Q5 model of total enthalpy was developed by Chen *et al.* [32] and Lu *et al.* [33] independently for higher computational efficiency. Both the D2Q9 and D2Q5 models have been successfully applied to simulate conjugate heat transfer problems [34,35]. Recently, a D3Q7 model of total enthalpy was further proposed by Li *et al.* [36], Lu *et al.* [37], and Hosseini *et al.* [38] for simulation of 3D solid-liquid phase change with a simple boundary. Since the energy equation of conjugate heat transfer problems can be recovered exactly by this kind of model, the standard LBM can still be adopted to solve the multiphase/multicomponent system with different thermophysical properties without introducing any extra corrections. However, although the modified distribution model retains the unique merits of standard LBM, its drawbacks are also kept, such as tie-up between time step and grid spacing, limitation on uniform grids, and requirement of substantial virtual memory. It causes the effective simulation of 3D conjugate heat transfer problems with a curved boundary to still be challenging.

Recently, the lattice Boltzmann flux solver (LBFS) was proposed by Shu and co-workers [39,40] to effectively remove the above drawbacks of standard LBM. LBFS is a finite-volume solver based on the local solution of the Boltzmann equation for evaluation of numerical fluxes at the cell interface. Specifically, the macroscopic governing equations are solved directly in LBFS, and the numerical fluxes are evaluated in a mesoscopic way by the local solution of lattice Boltzmann equation at the cell interface. Since the lattice Boltzmann solution at each cell interface is independent of each other and the streaming time step is unrelated to the marching time step for solving the macroscopic governing equations, the LBFS applies very well to nonuniform mesh and curved boundaries. Besides, the virtual memory for distribution functions is avoided in LBFS to conserve the virtual memory, especially for 3D scenarios. Due to its distinguishing features, the LBFS has been widely used to simulate multiphase flows with large density ratio and high Reynolds number [41] and investigate variable property effects on the flow and heat transfer characteristics of natural convection in the horizontal concentric annulus [42]. By reconstructing the numerical flux of the energy equation via local solution of the Boltzmann equation with the D2Q9 model of Huang and Wu [31], Yang *et al.* [43] developed an LBFS for two-dimensional (2D) conjugate heat transfer problems and validated its accuracy and flexibility by several test cases. In the present work, the previous LBFS is further extended to effectively simulate 3D fluid-solid conjugate heat transfer problems with

complicated geometry. At first, a Chapman-Enskog expansion analysis with the collision time as the expansion parameter for recovering the continuity, momentum, and energy equations is presented to reveal the connections between the macroscopic fluxes and solution of the LBE. Then, a 3D local coordinate system aligned to the normal direction and two tangential directions of the cell interface and a corresponding coordinate transformation from the local coordinate system to the global coordinate system are introduced to calculate the macroscopic fluxes at the cell interface. After that, the conservative variables at cell centers are updated by evolving the macroscopic governing equations in time. The performance of the developed method will be demonstrated by simulating steady and unsteady natural convection in a finned 3D cavity and in a finned 3D annulus.

II. LATTICE BOLTZMANN MODELS AND CHAPMAN-ENSKOG EXPANSION ANALYSIS

According to kinetic theory, the macroscopic governing equations can be recovered from the Boltzmann equation with a continuum assumption. In this process, the relationships between the two systems can be established. LBFS is actually based on these relationships to reconstruct the numerical fluxes of macroscopic governing equations. For the incompressible fluid-solid conjugate heat transfer problems considered in this work, two Boltzmann equations with the Bhatnagar-Gross-Krook (BGK) approximation are commonly used:

$$\frac{\partial f_i}{\partial t} + \mathbf{e}_i \cdot \nabla f_i = \frac{f_i^{\text{eq}} - f_i}{\tau_\mu}, \quad (1)$$

$$\frac{\partial g_i}{\partial t} + \mathbf{e}_i \cdot \nabla g_i = \frac{g_i^{\text{eq}} - g_i}{\tau_\kappa}, \quad (2)$$

where f_i and g_i are the density distribution function and the total enthalpy distribution function along the direction of discrete velocity \mathbf{e}_i . f_i^{eq} and g_i^{eq} are the equilibrium states approached by f_i and g_i through particle collision within the collision timescales τ_μ and τ_κ , respectively. Equation (1) is used to recover the continuity and momentum equations, and Eq. (2) is utilized to recover the energy equation.

In this work, a 15-bit lattice velocity model (D3Q15) is used for the density distribution function, which is given by

$$f_i^{\text{eq}} = \rho \omega_i \left[1 + \frac{\mathbf{e}_i \cdot \mathbf{u}}{c_s^2} + \frac{(\mathbf{e}_i \mathbf{e}_i - c_s^2 \mathbf{I}) : \mathbf{u} \mathbf{u}}{2c_s^4} \right], \quad (3a)$$

$$\mathbf{e}_i = \begin{cases} (0, 0, 0)^T, & i = 0 \\ (\pm 1, 0, 0)^T, (0, \pm 1, 0)^T, (0, 0, \pm 1)^T, & i = 1 \sim 6, \\ (\pm 1, \pm 1, \pm 1)^T, & i = 7 \sim 14 \end{cases} \quad (3b)$$

where ρ is the density and \mathbf{u} is the velocity vector of the mean flow, \mathbf{I} is the unit tensor, ω_i denotes the weight coefficient, and c_s represents the sound speed. In the D3Q15 model, $\omega_0 = 2/9$, $\omega_{1\sim 6} = 1/9$, $\omega_{7\sim 14} = 1/72$, and $c_s = 1/\sqrt{3}$.

For the total enthalpy distribution function, a seven-bit lattice velocity model (D3Q7) is utilized, which is given

by [36]

$$g_i^{\text{eq}} = \begin{cases} C_p T - C_{p,0} T + \omega_i C_{p,0} T, & i = 0 \\ \omega_i T [C_{p,0} + 4C_p \mathbf{e}_i \cdot \mathbf{u}], & i \neq 0 \end{cases} \quad (4a)$$

$$\mathbf{e}_i = \begin{cases} (0, 0, 0)^T, & i = 0 \\ (\pm 1, 0, 0)^T, (0, \pm 1, 0)^T, (0, 0, \pm 1)^T, & i = 1 \sim 6 \end{cases} \quad (4b)$$

The corresponding weight coefficients have values of $\omega_0 = 1/4$ and $\omega_{1\sim 6} = 1/8$. T is the temperature, and C_p is the specific heat at constant pressure. $C_{p,0}$ denotes the reference specific heat, which remains unvaried in the whole domain.

First, we seek the connections between Eq. (1) and the continuity and momentum equations through the Chapman-Enskog expansion analysis. From the D3Q15 model, the following relationships can be obtained:

$$\rho = \sum_i f_i^{\text{eq}}, \quad (5a)$$

$$\rho u_\alpha = \sum_i \mathbf{e}_{i,\alpha} f_i^{\text{eq}}, \quad (5b)$$

$$\rho u_\alpha u_\beta + \rho c_s^2 \delta_{\alpha\beta} = \sum_i \mathbf{e}_{i,\alpha} \mathbf{e}_{i,\beta} f_i^{\text{eq}}, \quad (5c)$$

$$\rho c_s^2 (u_\alpha \delta_{\beta\chi} + u_\beta \delta_{\chi\alpha} + u_\chi \delta_{\alpha\beta}) = \sum_i \mathbf{e}_{i,\alpha} \mathbf{e}_{i,\beta} \mathbf{e}_{i,\chi} f_i^{\text{eq}}, \quad (5d)$$

where $\mathbf{e}_{i,\alpha}$, $\mathbf{e}_{i,\beta}$, $\mathbf{e}_{i,\chi}$ and u_α , u_β , u_χ are the components of particle velocity and macroscopic flow velocity in the α , β , and χ direction, respectively. In addition, according to the compatibility condition, we know that the collision term does not make contributions to the calculation of conservative variables, which yields

$$\sum_i \boldsymbol{\varphi}_i (f_i^{\text{eq}} - f_i) = \sum_i \boldsymbol{\varphi}_i \tau_\mu D f_i = \mathbf{0}, \quad (6)$$

where $\boldsymbol{\varphi}_i = (1, \mathbf{e}_i)^T$ stands for the moment vector and $D f_i = (\partial_t + \mathbf{e}_i \cdot \nabla) f_i$ is the substantial derivative of the distribution function f_i .

According to the Chapman-Enskog expansion analysis, to recover Navier-Stokes equations, the distribution function can be expanded to the first order of the collision time as follows:

$$f_i = f_i^{\text{eq}} - \tau_\mu D f_i = f_i^{\text{eq}} - \tau_\mu D f_i^{\text{eq}} + O(\tau_\mu^2). \quad (7)$$

Note that the expression of $f_i = f_i^{\text{eq}} - \tau_\mu D f_i$ [i.e., Eq. (1)] has been substituted into $D f_i$ to derive the above expression. Applying the operator D to Eq. (7), we can get

$$D f_i = D f_i^{\text{eq}} - D(\tau_\mu D f_i^{\text{eq}}) + O(\tau_\mu^2). \quad (8)$$

By multiplying $\boldsymbol{\varphi}_i$ on both sides of Eq. (8) and performing a summation over the particle velocity space for the resultant equation yields

$$\begin{aligned} & \partial_t \sum_i \boldsymbol{\varphi}_i f_i^{\text{eq}} + \nabla \cdot \sum_i \mathbf{e}_i \boldsymbol{\varphi}_i f_i^{\text{eq}} \\ &= \partial_t \sum_i \boldsymbol{\varphi}_i \tau_\mu D f_i^{\text{eq}} + \nabla \cdot \sum_i \mathbf{e}_i \boldsymbol{\varphi}_i \tau_\mu D f_i^{\text{eq}} + O(\tau_\mu^2). \end{aligned} \quad (9)$$

Note that the compatibility condition has been used in deriving the above equation. By substituting Eq. (7) into the

first term on the right-hand side of Eq. (9) and utilizing the compatibility condition, we can obtain

$$\partial_t \sum_i \boldsymbol{\varphi}_i f_i^{\text{eq}} + \nabla \cdot \sum_i \mathbf{e}_i \boldsymbol{\varphi}_i f_i^{\text{eq}} = \nabla \cdot \sum_i \mathbf{e}_i \boldsymbol{\varphi}_i \tau_\mu D f_i^{\text{eq}} + O(\tau_\mu^2). \quad (10)$$

The first component of $\boldsymbol{\varphi}_i$ is 1, which gives the following relationship when being substituted into Eq. (10):

$$\partial_t \sum_i f_i^{\text{eq}} + \nabla \cdot \sum_i \mathbf{e}_i f_i^{\text{eq}} = \nabla \cdot \sum_i \mathbf{e}_i \tau_\mu D f_i^{\text{eq}} + O(\tau_\mu^2), \quad (11)$$

Utilizing Eqs. (5a), (5b), (7), and the compatibility condition (6), the above equation can be rewritten as

$$\partial_t \rho + \nabla \cdot (\rho \mathbf{u}) = O(\tau_\mu^2), \quad (12)$$

which recovers the continuity equation in the order of $O(\tau_\mu^2)$.

Considering the second component of $\boldsymbol{\varphi}_i$ in Eq. (10) gives

$$\begin{aligned} & \partial_t \sum_i \mathbf{e}_i f_i^{\text{eq}} + \nabla \cdot \sum_i \mathbf{e}_i \mathbf{e}_i f_i^{\text{eq}} \\ &= \nabla \cdot \left[\tau_\mu \left(\partial_t \sum_i \mathbf{e}_i \mathbf{e}_i f_i^{\text{eq}} + \nabla \cdot \sum_i \mathbf{e}_i \mathbf{e}_i \mathbf{e}_i f_i^{\text{eq}} \right) \right] + O(\tau_\mu^2). \end{aligned} \quad (13)$$

Substituting the conservative relationships in Eqs. (5b) and (5c) into the left-hand side of Eq. (13), we have

$$\partial_t (\rho \mathbf{u}) + \nabla \cdot (\rho \mathbf{u} \mathbf{u} + p \mathbf{I}) = O(\tau_\mu), \quad (14)$$

where $p = \rho c_s^2$ is the pressure. Furthermore, substituting the conservative relationships in Eqs. (5c) and (5d) into the right-hand side of Eq. (13) yields

$$\begin{aligned} & \partial_t \sum_i \mathbf{e}_i \mathbf{e}_i f_i^{\text{eq}} \\ &= \partial_t (\rho \mathbf{u} \mathbf{u} + p \mathbf{I}) \\ &= \partial_t (\rho \mathbf{u}) \mathbf{u} + \mathbf{u} \partial_t (\rho \mathbf{u}) - \mathbf{u} \mathbf{u} \partial_t \rho + c_s^2 \partial_t \rho \mathbf{I} \\ &= -\nabla \cdot (\rho \mathbf{u} \mathbf{u} \mathbf{u}) - [(\nabla p) \mathbf{u} + \mathbf{u} \nabla p] - \nabla \cdot (\rho \mathbf{u}) \mathbf{I} + O(\tau_\mu), \end{aligned} \quad (15a)$$

$$\begin{aligned} & \nabla \cdot \sum_i \mathbf{e}_i \mathbf{e}_i \mathbf{e}_i f_i^{\text{eq}} \\ &= \partial_\chi [p(u_\alpha \delta_{\beta\chi} + u_\beta \delta_{\chi\alpha} + u_\chi \delta_{\alpha\beta})] \\ &= p[\nabla \mathbf{u} + (\nabla \mathbf{u})^T] + [(\nabla p) \mathbf{u} + \mathbf{u} \nabla p] + \nabla \cdot (\rho \mathbf{u}) \mathbf{I}. \end{aligned} \quad (15b)$$

Note that Eqs. (12) and (14) have been used for derivation of Eq. (15a). Although the truncation error of Eq. (15a) is $O(\tau_\mu)$, it is multiplied by τ_μ when being substituted into Eq. (13). Thus, the approximation in Eq. (15a) will not affect the overall accuracy of Eq. (13), which yields

$$\begin{aligned} & \partial_t (\rho \mathbf{u}) + \nabla \cdot (\rho \mathbf{u} \mathbf{u} + p \mathbf{I}) \\ &= \nabla \cdot \{ \mu [\nabla \mathbf{u} + (\nabla \mathbf{u})^T] \} + O(\tau_\mu^2, \tau_\mu |\mathbf{u}|^3), \end{aligned} \quad (16)$$

where the dynamic viscosity μ is connected to the collision time τ_μ by

$$\tau_\mu = \frac{\mu}{p} = \frac{\mu}{\rho c_s^2}. \quad (17)$$

Equation (16) proves that the momentum equation can be recovered from the Boltzmann equation in the order of $O(\tau_\mu^2, \tau_\mu |\mathbf{u}|^3)$.

Second, we seek the connections between Eq. (2) and the energy equation of conjugate heat transfer problems. From the D3Q7 model, the following conservative relationships can be obtained:

$$C_p T = \sum_i g_i^{\text{eq}}, \quad (18a)$$

$$C_p T u_\alpha = \sum_i \mathbf{e}_{i,\alpha} g_i^{\text{eq}}, \quad (18b)$$

$$\frac{1}{4} C_{p,0} T \delta_{\alpha\beta} = \sum_i \mathbf{e}_{i,\alpha} \mathbf{e}_{i,\beta} g_i^{\text{eq}}. \quad (18c)$$

After a similar derivation process to Eq. (10), we have

$$\partial_t \sum_i g_i^{\text{eq}} + \nabla \cdot \sum_i \mathbf{e}_i g_i^{\text{eq}} = \nabla \cdot \sum_i \mathbf{e}_i \tau_\kappa D g_i^{\text{eq}} + O(\tau_\kappa^2). \quad (19)$$

Substituting Eqs. (18a)–(18c) into Eq. (19) and neglecting the higher order term $\nabla \cdot [\tau_\kappa \partial_t (C_p T \mathbf{u})]$, we can get

$$\partial_t (C_p T) + \nabla \cdot (C_p T \mathbf{u}) = \nabla \cdot \left\{ \frac{\tau_\kappa}{4} \nabla (C_{p,0} T) \right\}. \quad (20)$$

Since $C_{p,0}$ is a constant, Eq. (20) can be reformulated as

$$\partial_t (C_p T) + \nabla \cdot (C_p T \mathbf{u}) = \nabla \cdot \left(\frac{\kappa}{\rho_0} \nabla T \right). \quad (21)$$

As a result, the thermal conductivity can be expressed by

$$\tau_\kappa = \frac{4\kappa}{\rho_0 C_{p,0}}. \quad (22)$$

Here ρ_0 is the reference density, which is set as $\rho_0 = 1$ in our simulations.

It should be noted that the collision time is used in the above analysis as the expansion parameter. This strategy is different from many LBM studies [14]. Since the expansions to the temporal derivative and the spatial derivative are avoided, the present analysis is more concise than that of the conventional LBM. Equations (10) and (19) suggest that one can use $f_i^{\text{eq}} - \tau_\mu D f_i^{\text{eq}}$ to reconstruct the numerical fluxes at the cell interface of continuity and momentum equations and utilize $g_i^{\text{eq}} - \tau_\kappa D g_i^{\text{eq}}$ to compute the flux of the energy equation. These relations are the foundation of the present scheme for calculation of macroscopic numerical fluxes.

III. LATTICE BOLTZMANN FLUX SOLVER FOR 3D CONJUGATE HEAT TRANSFER PROBLEMS

A. Finite-volume discretization of 3D macroscopic governing equations

In the context of LBM and LBFS, the macroscopic governing equations for incompressible fluid-solid conjugate heat transfer problems can be written as [44]

$$\frac{\partial \rho}{\partial t} + \nabla \cdot (\rho \mathbf{u}) = 0, \text{ in the flow domain,} \quad (23)$$

$$\begin{aligned} \frac{\partial \rho \mathbf{u}}{\partial t} + \nabla \cdot (\rho \mathbf{u} \mathbf{u} + p \mathbf{I}) \\ = \nabla \cdot \{ \mu [\nabla \mathbf{u} + (\nabla \mathbf{u})^T] \} + \mathbf{f}_E, \text{ in the flow domain,} \end{aligned} \quad (24)$$

$$\begin{aligned} \frac{\partial C_p T}{\partial t} + \nabla \cdot (C_p T \mathbf{u}) \\ = \nabla \cdot \left(\frac{\kappa}{\rho_0} \nabla T \right), \text{ in both the flow and solid domains,} \end{aligned} \quad (25)$$

where \mathbf{f}_E denotes the buoyancy force, which is calculated by the Boussinesq approximation,

$$\mathbf{f}_E = -\rho \beta (T - T_m) g \mathbf{j}. \quad (26)$$

Here, β is the thermal expansion coefficient, T_m is the average temperature, g is the gravity acceleration, and \mathbf{j} is the unit vector in the y direction.

Due to its geometric flexibility, the finite-volume method is chosen to discretize Eqs. (23)–(25), and the conservative variables are defined at the cell centers, which yield

$$\frac{d\mathbf{W}_I}{dt} = -\frac{1}{\Omega_I} \sum_{j=1}^{N_f} \mathbf{F}_{nj} S_j + \mathbf{Q}_I, \quad (27)$$

where I is the index of control volume, and Ω_I and N_f represent the volume and the number of faces of the control volume I , respectively. S_j denotes the area of the j th interface of control volume. For the 3D case, the conservative variable vector \mathbf{W} , flux vector \mathbf{F}_n , and source term \mathbf{Q} are given by

$$\mathbf{W} = (\rho, \rho u, \rho v, \rho w, C_p T)^T, \quad (28)$$

$$\mathbf{F}_n = (F_\rho, F_{\rho u}, F_{\rho v}, F_{\rho w}, F_T)^T, \quad (29)$$

$$\mathbf{Q} = [0, 0, -\rho \beta (T - T_m) g, 0, 0]^T. \quad (30)$$

Here, u , v , and w are the velocity components in the x , y , and z direction, respectively. In order to solve Eq. (27), the numerical fluxes \mathbf{F}_n and the source term \mathbf{Q} have to be determined first. When an explicit method is adopted, \mathbf{Q} can be calculated directly from the conservative variables \mathbf{W} at cell centers. Thus, the only remaining task is to compute the fluxes \mathbf{F}_n .

For the convenience of derivation and application, a local coordinate system defined on the cell interface is introduced in this work. In the local coordinate system, the x_1 axis is taken

as the normal direction pointing outwards of the cell interface, while the x_2 axis and x_3 axis are chosen as two tangential directions of the cell interface, which are mutually orthogonal and form a right-hand coordinate system. These axes are also consistent with the lattice velocities in the off-diagonal directions. The conservative variables and numerical fluxes expressed in the local coordinate system are defined as

$$\bar{\mathbf{W}} = (\rho, \rho u_1, \rho u_2, \rho u_3, C_p T)^T \quad (31)$$

$$\bar{\mathbf{F}}_n = (F_\rho, F_{\rho u_1}, F_{\rho u_2}, F_{\rho u_3}, F_T)^T \quad (32)$$

where u_1 , u_2 , and u_3 are the velocity components in the x_1 , x_2 , and x_3 direction, respectively. The conservative variables and numerical fluxes expressed in two coordinate systems are correlated by following transformations:

$$\begin{aligned} u &= n_{1x}u_1 + n_{2x}u_2 + n_{3x}u_3, \\ v &= n_{1y}u_1 + n_{2y}u_2 + n_{3y}u_3, \end{aligned} \quad (33a)$$

$$\begin{aligned} w &= n_{1z}u_1 + n_{2z}u_2 + n_{3z}u_3 \\ F_{\rho u} &= n_{1x}F_{\rho u_1} + n_{2x}F_{\rho u_2} + n_{3x}F_{\rho u_3}, \\ F_{\rho v} &= n_{1y}F_{\rho u_1} + n_{2y}F_{\rho u_2} + n_{3y}F_{\rho u_3}, \end{aligned} \quad (33b)$$

$$F_{\rho w} = n_{1z}F_{\rho u_1} + n_{2z}F_{\rho u_2} + n_{3z}F_{\rho u_3}$$

where $\mathbf{n}_1 = (n_{1x}, n_{1y}, n_{1z})$, $\mathbf{n}_2 = (n_{2x}, n_{2y}, n_{2z})$, and $\mathbf{n}_3 = (n_{3x}, n_{3y}, n_{3z})$ represent the unit vectors of the x_1 axis, x_2 axis, and the x_3 axis, respectively. Equations (33a) and (33b) suggest that the calculation of \mathbf{F}_n is equivalent to evaluating $\bar{\mathbf{F}}_n$ in the local coordinate system. In the following section, we will focus on the calculation of $\bar{\mathbf{F}}_n$.

B. Lattice Boltzmann flux solver for evaluation of fluxes at the cell interface

For simplicity, we denote the location of the cell interface as $\mathbf{r} = 0$. According to Eqs. (10) and (19), the numerical fluxes $\bar{\mathbf{F}}_n$ can be calculated by

$$\bar{\mathbf{F}}_n(1:4) = \sum_i \mathbf{e}_{i,1} \bar{\varphi}_i f_i(0, t), \quad (34)$$

$$\bar{\mathbf{F}}_n(5) = \sum_i \mathbf{e}_{i,1} g_i(0, t), \quad (35)$$

where $\bar{\mathbf{F}}_n(1:4)$ and $\bar{\mathbf{F}}_n(5)$ denote the first four components and the fifth component of the flux vector $\bar{\mathbf{F}}_n$, respectively. $\bar{\varphi}_i = (1, \mathbf{e}_{i,1}, \mathbf{e}_{i,2}, \mathbf{e}_{i,3})^T$ is the moment vector, where $\mathbf{e}_{i,1}$, $\mathbf{e}_{i,2}$, and $\mathbf{e}_{i,3}$ are the components of particle velocity expressed in the local coordinate system. $f_i(0, t)$ and $g_i(0, t)$ are respectively the density distribution function and the total enthalpy distribution function at the cell interface truncated to $O(\tau_\mu^2)$ and $O(\tau_\kappa^2)$, which are given by

$$f_i(0, t) = f_i^{\text{eq}}(0, t) - \tau_\mu D f_i^{\text{eq}}(0, t), \quad (36)$$

$$g_i(0, t) = g_i^{\text{eq}}(0, t) - \tau_\kappa D g_i^{\text{eq}}(0, t). \quad (37)$$

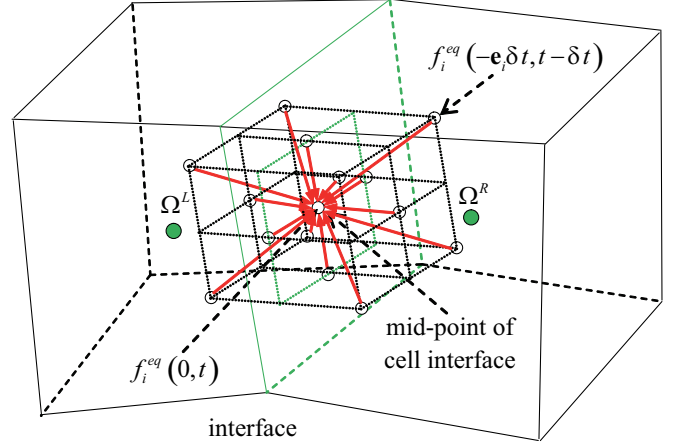


FIG. 1. Distribution of equilibrium functions at the cell interface and its surrounding points (D3Q15 model for illustration).

By using the backward difference method to operator D , the above equations can be approximated by

$$f_i(0, t) = f_i^{\text{eq}}(0, t) + \frac{\tau_\mu}{\delta t} [f_i^{\text{eq}}(-\mathbf{e}_i \delta t, t - \delta t) - f_i^{\text{eq}}(0, t)], \quad (38)$$

$$g_i(0, t) = g_i^{\text{eq}}(0, t) + \frac{\tau_\kappa}{\delta t} [g_i^{\text{eq}}(-\mathbf{e}_i \delta t, t - \delta t) - g_i^{\text{eq}}(0, t)]. \quad (39)$$

Here $f_i^{\text{eq}}(0, t)$ and $g_i^{\text{eq}}(0, t)$ are the equilibrium distribution functions at the cell interface, and $f_i^{\text{eq}}(-\mathbf{e}_i \delta t, t - \delta t)$ and $g_i^{\text{eq}}(-\mathbf{e}_i \delta t, t - \delta t)$ are the equilibrium distribution functions at the surrounding points of the cell interface, as shown in Fig. 1. δt is the streaming time step, which can be determined by [43]

$$\delta t = \frac{0.4 \times \min\{\Delta l, \Delta r\}}{\max_i(|\mathbf{e}_i|)} = 0.4 \times \min\{\Delta l, \Delta r\}, \quad (40)$$

where Δl and Δr are the shortest edge length of the left and right cells around the cell interface, respectively.

From the above analysis, the key to compute the numerical fluxes $\bar{\mathbf{F}}_n$ is to calculate the equilibrium states at the cell interface and its surrounding points, which are the functions of flow variables at the corresponding physical locations. For any variable ϕ , its value at the surrounding point of the cell interface can be computed by

$$\phi(-\mathbf{e}_i \delta t, t - \delta t) = \begin{cases} \phi^L - \nabla \phi^L \cdot \mathbf{e}_i \delta t, & \text{if } \mathbf{e}_{i,1} > 0 \\ \phi^R - \nabla \phi^R \cdot \mathbf{e}_i \delta t, & \text{if } \mathbf{e}_{i,1} < 0, \\ \phi^M - \nabla \phi^M \cdot \mathbf{e}_i \delta t, & \text{if } \mathbf{e}_{i,1} = 0 \end{cases} \quad (41)$$

where ϕ represents the variables of ρ , u_1 , u_2 , u_3 , and T . $\nabla \phi$ is the first-order derivative of ϕ . The superscripts "L" and "R" denote the values at the left and right sides of cell interface, and the superscript "M" represents the arithmetic mean at the cell interface. Once ρ , u_1 , u_2 , u_3 , and T at the surrounding points of the cell interface are obtained, $f_i^{\text{eq}}(-\mathbf{e}_i \delta t, t - \delta t)$ and $g_i^{\text{eq}}(-\mathbf{e}_i \delta t, t - \delta t)$ can be computed by substituting Eq. (41) into Eqs. (3a) and Eq. (4a), respectively.

For the flow variables at the cell interface, they can be calculated by the compatibility condition. By taking moments of Eqs. (38) and (39), we have

$$\overline{\mathbf{W}}^{\text{face}}(1:4) = \sum_i \bar{\varphi}_i f_i^{\text{eq}}(0, t) = \sum_i \bar{\varphi}_i f_i^{\text{eq}}(-\mathbf{e}_i \delta t, t - \delta t), \quad (42)$$

$$\overline{\mathbf{W}}^{\text{face}}(5) = \sum_i g_i^{\text{eq}}(0, t) = \sum_i g_i^{\text{eq}}(-\mathbf{e}_i \delta t, t - \delta t), \quad (43)$$

where $\overline{\mathbf{W}}^{\text{face}}(1:4)$ and $\overline{\mathbf{W}}^{\text{face}}(5)$ denote the first four components and the fifth component of the conservative variable vector at the cell interface, respectively. Since $f_i^{\text{eq}}(-\mathbf{e}_i \delta t, t - \delta t)$ and $g_i^{\text{eq}}(-\mathbf{e}_i \delta t, t - \delta t)$ have been determined previously, $\overline{\mathbf{W}}^{\text{face}}$ can be computed uniquely from Eqs. (42) and (43). After that, we can calculate $f_i^{\text{eq}}(0, t)$ and $g_i^{\text{eq}}(0, t)$ by substituting $\overline{\mathbf{W}}^{\text{face}}$ into Eqs. (3a) and (4a), respectively.

For the incompressible fluid-solid conjugate heat transfer problems, the value of thermal conductivity κ changes suddenly at the conjugate interface. Thus, an appropriate method should be introduced to calculate its value in such circumstances. In our previous work [43], the thermal conductivity at the cell interface is computed with the aid of the concept of thermal resistance, which yields

$$\tau_\kappa^M = \frac{\kappa^L \kappa^R (r^L + r^R)}{\kappa^R r^L + \kappa^L r^R}, \quad (44)$$

where r denotes the distances of cell center to cell interface. Once the thermal conductivity at the cell interface is obtained, τ_κ in Eq. (39) can then be computed by

$$\tau_\kappa = \frac{4\kappa^M}{\rho_0 C_{p,0}}. \quad (45)$$

This treatment has been shown to be effective for both steady and unsteady flows.

IV. NUMERICAL EXAMPLES

In this section, the unsteady heat conduction in an infinite system filled with two media and the natural convection in a finned 3D cavity and in a finned 3D annulus are simulated to validate the present solver. According to the suggestion of Huang and Wu [31], the harmonic mean is used to calculate the reference specific heat, i.e., $C_{p,0} = 2C_{p,1}C_{p,2}/[C_{p,1} + C_{p,2}]$, where $C_{p,1}$ and $C_{p,2}$ are the specific heats of different media. The convergence criterion of all test cases is set to be

$$\text{Error} = \max(V_{\text{error}}, T_{\text{error}}) < 1 \times 10^{-8}, \quad (46)$$

where V_{error} and T_{error} are the relative error of the velocity distribution and temperature distribution, which are computed by

$$V_{\text{error}} = \frac{\sum_i \sqrt{(u_i^{n+1} - u_i^n)^2 + (v_i^{n+1} - v_i^n)^2 + (w_i^{n+1} - w_i^n)^2}}{\sum_i \sqrt{(u_i^{n+1})^2 + (v_i^{n+1})^2 + (w_i^{n+1})^2}}, \quad (47a)$$

$$T_{\text{error}} = \frac{\sum_i |T_i^{n+1} - T_i^n|}{\sum_i T_i^{n+1}}. \quad (47b)$$

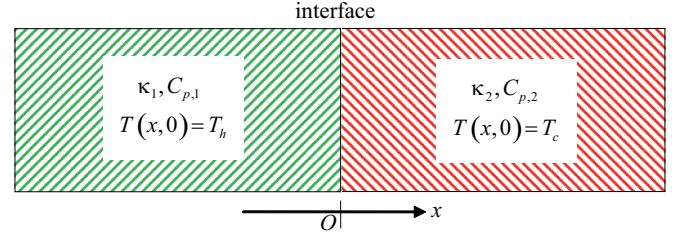


FIG. 2. Schematic of unsteady heat conduction in an infinite system.

In addition, the explicit Euler method is adopted to solve Eq. (27), and the Courant-Friedrichs-Lewy (CFL) number is taken as 0.1.

Case 1: Unsteady heat conduction in an infinite system

In this section, the unsteady heat conduction in an infinite system filled with two media is simulated to assess the numerical accuracy of the present solver. As shown in Fig. 2, the initial temperatures of medium 1 and medium 2 are set as T_h and T_c , respectively. The ratios of the heat conductivity and the specific heat are taken as $\kappa_1/\kappa_2 = 1/4$ and $C_{p,1}/C_{p,2} = 1/16$, respectively. Under such conditions, the analytical solution of this problem can be written as [31,33]

$$T(x, t) = \begin{cases} T_h - \frac{(T_h - T_c) \sqrt{\kappa_2 C_{p,2}}}{\sqrt{\kappa_1 C_{p,1}} + \sqrt{\kappa_2 C_{p,2}}} \operatorname{erfc}\left(\frac{-x}{2\sqrt{\kappa_1 t / C_{p,1}}}\right), & x \leq 0 \\ T_c + \frac{(T_h - T_c) \sqrt{\kappa_1 C_{p,1}}}{\sqrt{\kappa_1 C_{p,1}} + \sqrt{\kappa_2 C_{p,2}}} \operatorname{erfc}\left(\frac{x}{2\sqrt{\kappa_2 t / C_{p,2}}}\right), & x \geq 0. \end{cases} \quad (48)$$

Here, $\operatorname{erfc}(x) = \frac{2}{\sqrt{\pi}} \int_x^{+\infty} e^{-\eta^2} d\eta$ is the complementary error function. In addition, to measure the numerical accuracy of the present method, the following relative error of the temperature distribution is calculated:

$$\text{Error} = \frac{\sqrt{\sum_{i=1}^{N_x} (T_i^a - T_i^c)^2}}{\sqrt{\sum_{i=1}^{N_x} (T_i^a)^2}}, \quad (49)$$

where T_i^a and T_i^c are respectively the analytical temperature and the calculated temperature at point i . N_x is the number of cells in the x direction. Four uniform meshes with $N_x = 20, 40, 80,$ and 160 are used to measure the relative error. In the y and z directions, the number of cells is fixed as 10. Figure 3 shows the relative error calculated by different meshes at time $t = 0.005$. It can be seen that the accuracy of the present solver is the second order in space.

Case 2: Steady and unsteady natural convection in a finned 3D cavity

The natural convection in a finned 3D cavity [45–47] is a good benchmark test to validate the effectiveness of the developed method for solving 3D incompressible fluid-solid conjugate heat transfer problems. The configuration of this problem is illustrated in Fig. 4. As can be seen in this figure, a rectangular conducting fin is centrally attached to the hot wall. The geometric parameters of the fin are set as $b/L = 0.5$, $s/L = 0.5$, and $e/L = 0.1$, where $L = 1$ is the characteristic length of the cubic cavity. On all walls of the cavity and the fin, the no-slip boundary condition is adopted. Except for the left

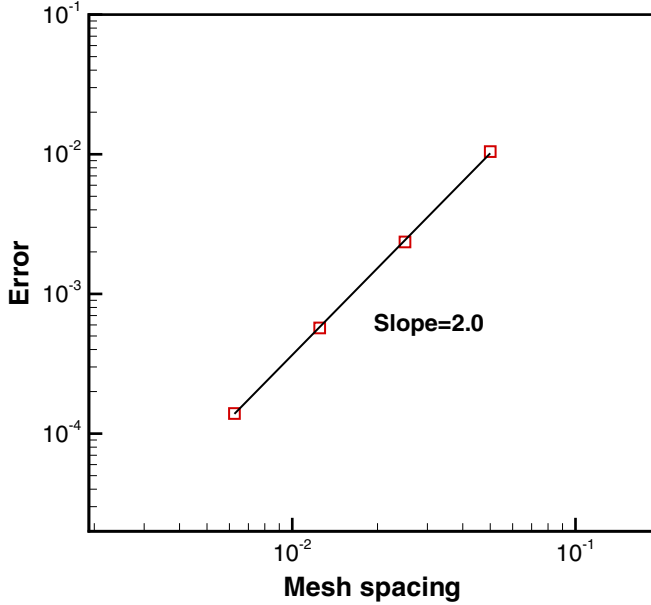


FIG. 3. Accuracy analysis of LBFS for unsteady heat conduction in an infinite system.

and right walls, which are set as the isothermal wall with fixed temperatures of $T_1 = 1$ and $T_0 = 0$, respectively, all walls of the cavity are treated as the adiabatic wall. The heat conductivity and the specific heat of the fluid are denoted as κ_1 and $C_{p,1}$, and those of the fin are defined as κ_2 and $C_{p,2}$. For simplicity, $R_\kappa = \kappa_2/\kappa_1$ and $R_C = C_{p,2}/C_{p,1}$ are introduced to represent the ratios of heat conductivity and specific heat for the fin and the fluid, respectively. In addition, the Prandtl number Pr and the Rayleigh number Ra , are defined as follows:

$$Pr = \frac{\nu}{\alpha_1}, \quad Ra = \frac{g\beta(T_1 - T_0)L^3}{\nu\alpha_1} = \frac{V_c^2 L^2}{\nu\alpha_1}, \quad (50)$$

where $\alpha_1 = \kappa_1/(\rho_0 C_{p,1})$ and $\nu = \mu/\rho_0$ are the thermal diffusivity and the kinematic viscosity of the fluid, respectively. $V_c = \sqrt{g\beta(T_1 - T_0)L}$ denotes the characteristic thermal velocity. To quantify the heat transfer efficiency of this problem, the

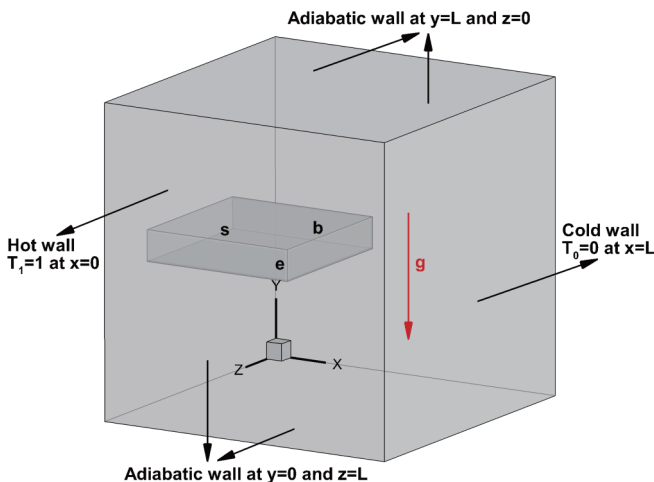


FIG. 4. Schematic of natural convection in a finned 3D cavity.

average Nusselt number on the hot wall is defined as follows:

$$\overline{Nu} = -\frac{R_\kappa L}{\xi(T_1 - T_0)L^2} \int_0^L \int_0^L \frac{\partial T}{\partial x} \Big|_{x=0} dydz, \quad (51)$$

where ξ is a coefficient which either equals R_κ for the bare area or equals 1 for the finned area of the hot wall. To be consistent with the work of Imani [47], we choose $R_\kappa = 10$, $V_c = 0.1$, and $Pr = 0.71$ in the present simulations, and the simulated Rayleigh numbers are changed from 10^3 to 10^6 . The computational domain is divided uniformly into $120 \times 120 \times 120$ cells.

At first, the steady case is simulated. When we reach steady-state fluid-solid heat transfer, only the thermal conductivity affects the temperature distribution [27]. Thus, the ratio of specific heat can be taken as $R_C = 1$ for simplicity. Figure 5 shows isothermal surfaces for steady natural convection in a finned 3D cavity at $Ra = 10^4$ and 10^6 . It can be seen that the existence of the fin alters the temperature distribution, and the effect is enhanced as the Rayleigh number increases. Figure 6 compares the computed temperature contours on the midplane of $z = 0.5$ at different Rayleigh numbers of $Ra = 10^3, 10^4, 10^5$, and 10^6 , with the results obtained by FLUENT. The u velocity profile along the vertical centerline and v velocity profile along the horizontal centerline on the midplane of $z = 0.5$ computed by the present solver and FLUENT are shown in Fig. 7, where $U_{ref} = \alpha_1/L$ is the reference velocity. Clearly, good agreements are achieved for both the temperature and velocity distributions. At $Ra = 10^3$, the magnitude of velocity is relatively small and the isotherms are nearly vertical. This means that the heat transfer is dominated by the thermal conduction in this case, which leads to relatively low heat transfer efficiency. In addition, the conduction along the fin displaces hot isotherms to the right due to its greater heat conductivity than the fluid. As the Rayleigh number is increased, the magnitude of velocity increases greatly and the isotherms are squeezed closer to the boundaries. At $Ra = 10^6$, distinct thermal stratification appears and more flow reaches the upper face of the fin, thereby enhancing the convection heat transfer at the upper part of the hot wall. This indicates that the heat transfer is dominated by the thermal convection in this case, which leads to relatively high heat transfer efficiency. These conclusions can be further verified via Table I, in which the computed average Nusselt numbers on the hot wall are compared with the data given by Frederick and Moraga [45] using the SIMPLER (semi-implicit method for pressure-linked equations, SIMPLE Revised) method, and Imani [47] applying the LBM and numerical simulation using FLUENT. Furthermore, Table II compares the percent contributions to overall heat transfer from the hot wall and fin faces calculated by different methods. It can be observed that the present results agree very well with the reference data.

Secondly, the unsteady case with $R_C = 20$ is tested to validate the performance of the present solver for simulation of fluid-solid conjugate heat transfer problems with different specific heats. Initially, the temperature is set as $(T_0 + T_1)/2$ and the velocity is taken as 0 in the whole computational domain. Figure 8 depicts the comparison of the computed temperature profiles along the horizontal centerline on the midplane of $z = 0.5$ at time $t = 0.01$ s, 0.02 s, and 0.05 s

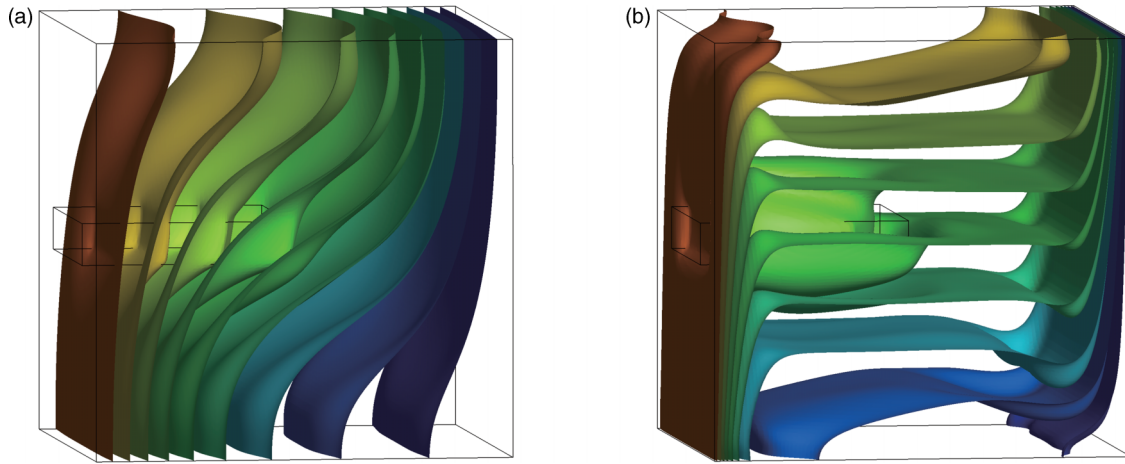


FIG. 5. Temperature contours for steady natural convection in a finned 3D cavity at (a) $Ra = 10^4$ and (b) $Ra = 10^6$.

with the results of FLUENT. In Fig. 9, the simulated u velocity profiles along the vertical centerline on the midplane of $z = 0.5$ at different instantaneous times are compared with the results of FLUENT. Clearly, the present results match very well with those of FLUENT. In addition, it can be seen from

Fig. 8 that the temperature distributions in the flow domain are affected significantly by the Rayleigh number due to heat convection, while the temperature distributions in the fin are basically the same for the four Rayleigh numbers considered here. As shown in Fig. 9, the peak velocity for the cases

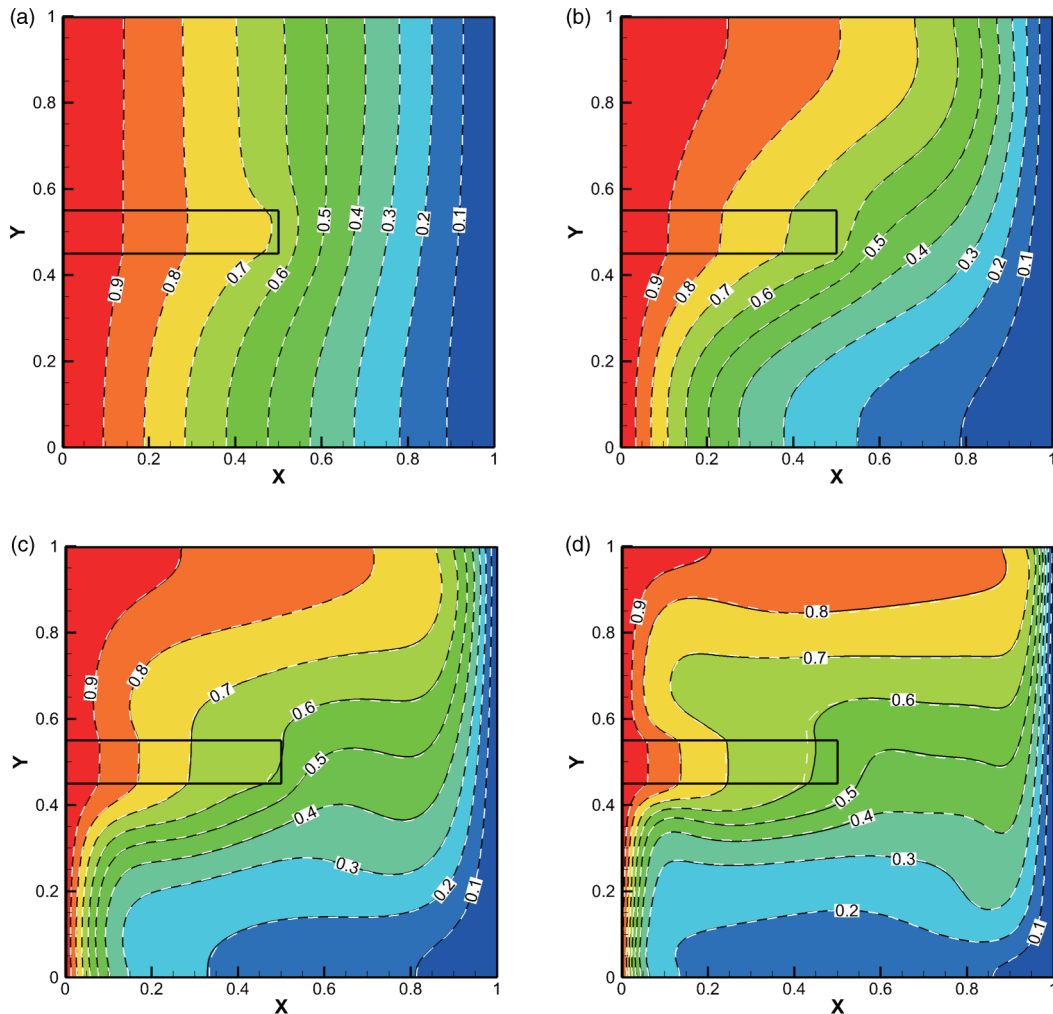


FIG. 6. Comparison of temperature contours at the $z = 0.5$ plane for steady natural convection in a finned 3D cavity at (a) $Ra = 10^3$, (b) $Ra = 10^4$, (c) $Ra = 10^5$, and (d) $Ra = 10^6$. (Present: colored background with black solid line; FLUENT: white dashed line.)

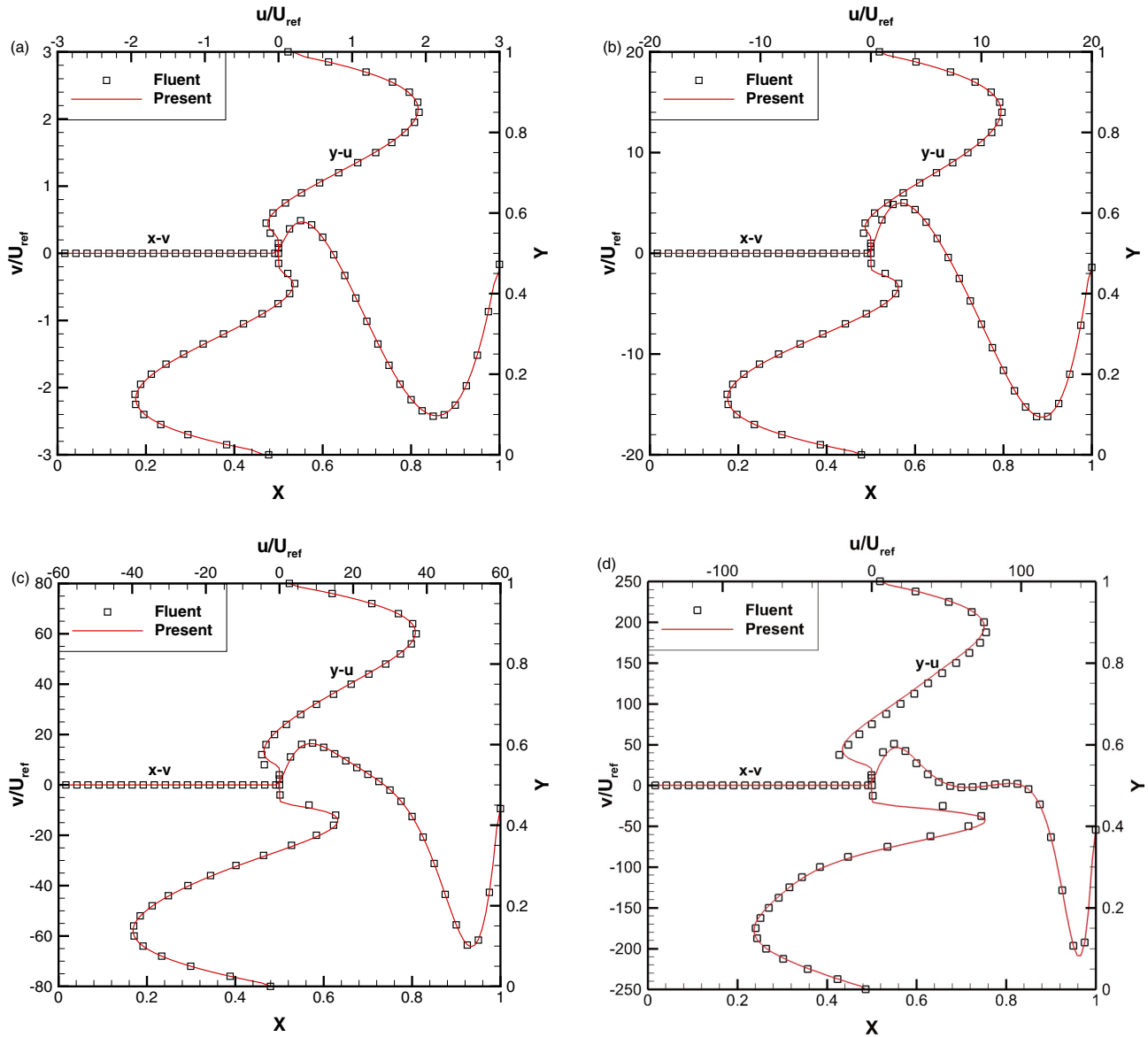


FIG. 7. Comparisons of u velocity profile along the vertical centerline and v velocity profile along the horizontal centerline at the $z = 0.5$ plane for steady natural convection in a finned 3D cavity at (a) $Ra = 10^3$, (b) $Ra = 10^4$, (c) $Ra = 10^5$, and (d) $Ra = 10^6$.

of $Ra = 10^5$ and 10^6 is not monotonically increased with time. This may be due to the fact that the heat convection is significantly stronger than the heat conduction in these cases. Thus, in the initial stage, the velocity field changes faster than the temperature field. In terms of the computational effort, the present solver requires 4.667 h to obtain the result at time $t = 0.01$ s for the case of $Ra = 10^4$, while the computation of

FLUENT requires 4.659 h. Note that the adaptive time stepping method is utilized in the simulation of FLUENT. This indicates that the computational efficiency of the present solver is comparable with that of FLUENT for simulation of unsteady flows.

Case 3: Steady and unsteady natural convection in a finned 3D annulus

TABLE I. Comparison of average Nusselt number on the hot wall for steady natural convection in a finned 3D cavity.

References	$Ra = 10^3$	$Ra = 10^4$	$Ra = 10^5$	$Ra = 10^6$
Frederick and Moraga [45]	1.167	1.781	4.256	8.612
Imani [47]	1.166	1.766	4.095	–
FLUENT	1.164	1.903	4.269	8.610
Present	1.164	1.895	4.255	8.547

TABLE II. Comparison of percent contributions to overall heat transfer from the hot wall and fin faces for steady natural convection in a finned 3D cavity.

Ra	References	Hot wall	Top	Bottom	Front	Sides
10^3	Frederick and Moraga [45]	68.119	5.337	10.179	11.941	4.424
	FLUENT	68.783	4.182	10.988	11.567	4.479
	Present	68.925	4.314	10.805	11.506	4.450
10^4	Frederick and Moraga [45]	69.870	-1.875	15.606	6.977	9.422
	FLUENT	74.919	-2.525	15.607	5.821	6.178
	Present	74.969	-2.468	15.483	5.841	6.174
10^5	Frederick and Moraga [45]	82.447	1.883	7.759	2.395	5.516
	FLUENT	83.651	1.576	7.910	2.172	4.691
	Present	83.763	1.606	7.767	2.194	4.671
10^6	Frederick and Moraga [45]	88.610	3.577	3.778	1.036	2.999
	FLUENT	88.835	3.441	3.615	0.964	3.146
	Present	88.983	3.472	3.501	0.981	3.062

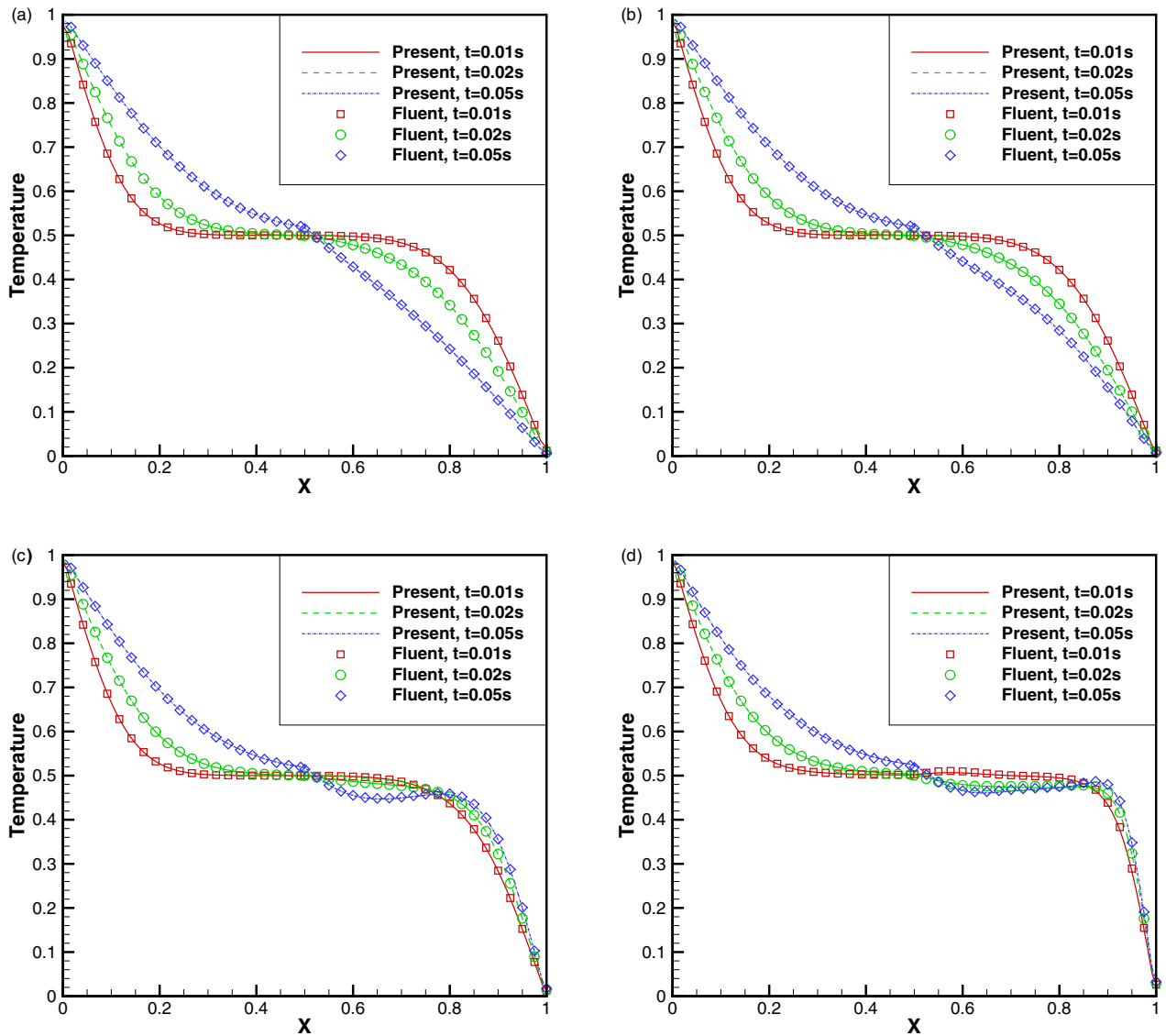


FIG. 8. Comparison of temperature profile along the horizontal centerline at $z = 0.5$ plane for unsteady natural convection in a finned 3D cavity at (a) $Ra = 10^3$, (b) $Ra = 10^4$, (c) $Ra = 10^5$, and (d) $Ra = 10^6$.

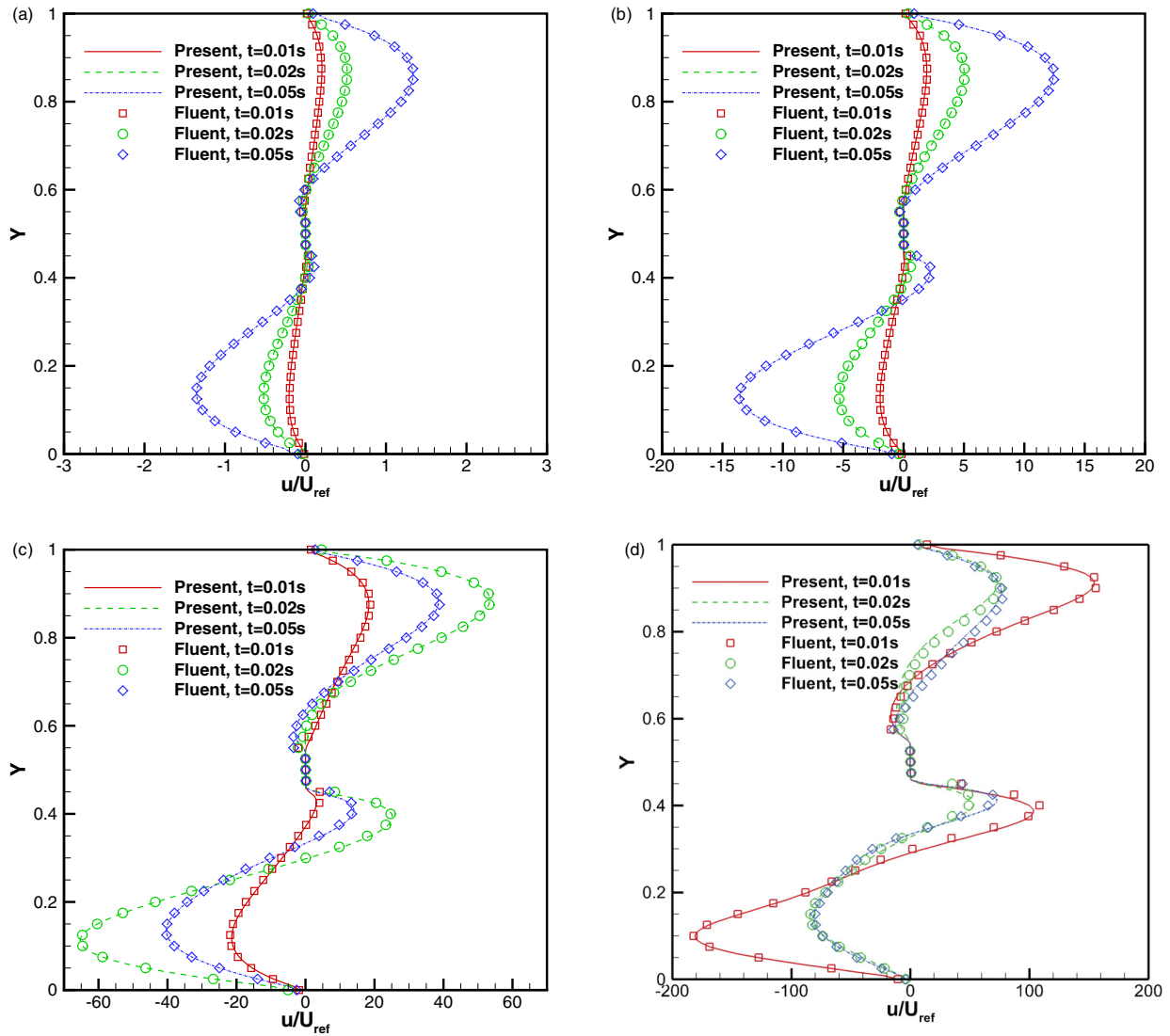


FIG. 9. Comparison of u velocity profile along the vertical centerline at the $z = 0.5$ plane for unsteady natural convection in a finned 3D cavity at (a) $Ra = 10^3$, (b) $Ra = 10^4$, (c) $Ra = 10^5$, and (d) $Ra = 10^6$.

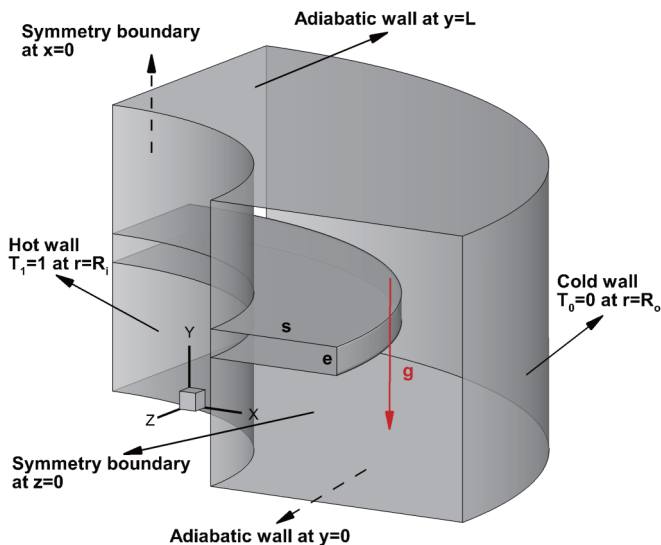


FIG. 10. Schematic of natural convection in a finned 3D annulus.

To validate the performance of the developed scheme on a nonuniform mesh and curved boundary, the steady and unsteady natural convection in a finned 3D annulus is simulated in this section. This test case is actually a variant of the axisymmetric natural convection in an annulus [48]. As shown in Fig. 10, the annulus consists of two coaxial vertical cylinders and two adiabatic walls at the top and bottom boundaries. The inner radius, outer radius, and the height of two cylinders are taken as $R_i = 1$, $R_o = 2$, and $L = 1$, respectively. The temperatures of the inner and the outer cylindrical surfaces are fixed at $T_1 = 1$ and $T_0 = 0$. A coaxial fin is centrally attached to the inner cylindrical surface. The geometric parameters of

TABLE III. Comparison of average Nusselt number on the hot wall for steady natural convection in a finned 3D annulus.

References	$Ra = 10^4$	$Ra = 10^5$
FLUENT	2.330	5.332
Present	2.322	5.325

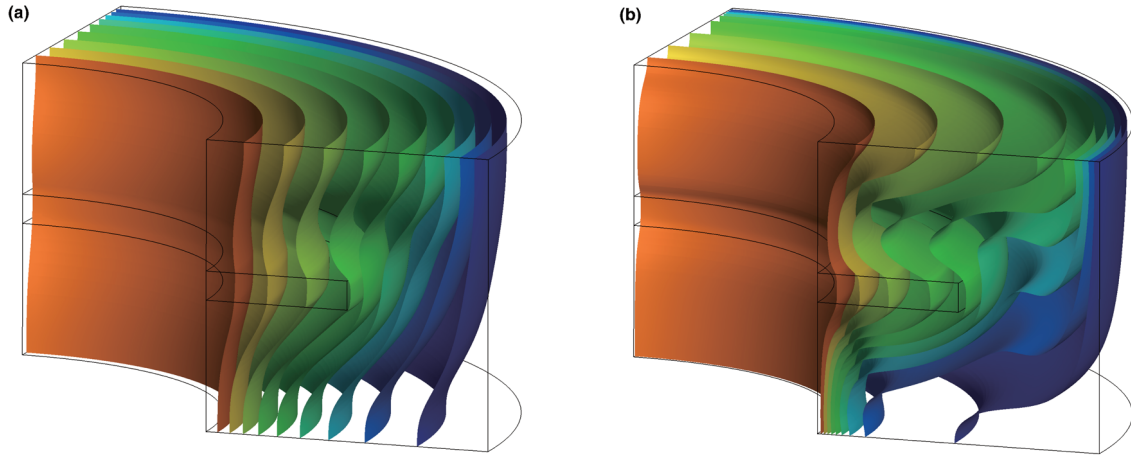


FIG. 11. Temperature contours for steady natural convection in a finned 3D annulus at (a) $Ra = 10^4$ and (b) $Ra = 10^5$.

the fin are set as $s/L = 0.5$ and $e/L = 0.1$. The thermophysical properties of the fluid and the fin are taken as $\kappa_1, C_{p,1}$ and $\kappa_2, C_{p,2}$, respectively. The ratios of heat conductivity and specific heat for the fin and the fluid are defined by $R_\kappa = \kappa_2/\kappa_1$ and $R_C = C_{p,2}/C_{p,1}$. The definitions of Prandtl number Pr and Rayleigh number Ra are the same as those in Eq. (50). In addition, the average Nusselt number on the inner cylindrical surface is defined as follows:

$$\overline{Nu} = -\frac{2R_i R_\kappa}{\pi \xi (T_1 - T_0)L} \int_0^{\pi/2} \int_0^L \left. \frac{\partial T}{\partial r} \right|_{r=R_i} dy d\theta, \quad (52)$$

where r and θ are the radial coordinate and the circumferential coordinate, respectively. Due to the symmetry of the geometry and the flow field, only a quarter of the annulus is simulated in the calculation and the symmetry condition is applied along the circumferential direction. In all simulations, we choose $R_\kappa = 10, V_c = 0.1$, and $Pr = 0.71$. The simulated Rayleigh numbers are taken as $Ra = 10^4$ and 10^5 . In addition, grid

points in the radial direction, the circumferential direction, and the axial direction are set as 101, 51, and 101, respectively.

At first, the steady case with $R_C = 1$ is simulated and the results are compared with those of FLUENT. Figure 11 shows the computed isothermal surfaces at $Ra = 10^4$ and 10^5 . Similar to the natural convection in a finned 3D cavity, the existence of the fin displaces hot isotherms to the cold wall, and the effect is enhanced as the Rayleigh number increases. The comparison of temperature contours on the $z = 0$ plane obtained by the present solver and FLUENT is depicted in Fig. 12, and the comparisons of the u velocity profile along the vertical centerline and v velocity profile along the horizontal centerline on the $z = 0$ plane are shown in Fig. 13. It can be seen that the present results agree very well with those of FLUENT. As compared with the natural convection in a finned 3D cavity, this test example has a greater peak negative u velocity above the fin for the same Rayleigh number, which indicates that the flow reaches the hot wall above the fin more

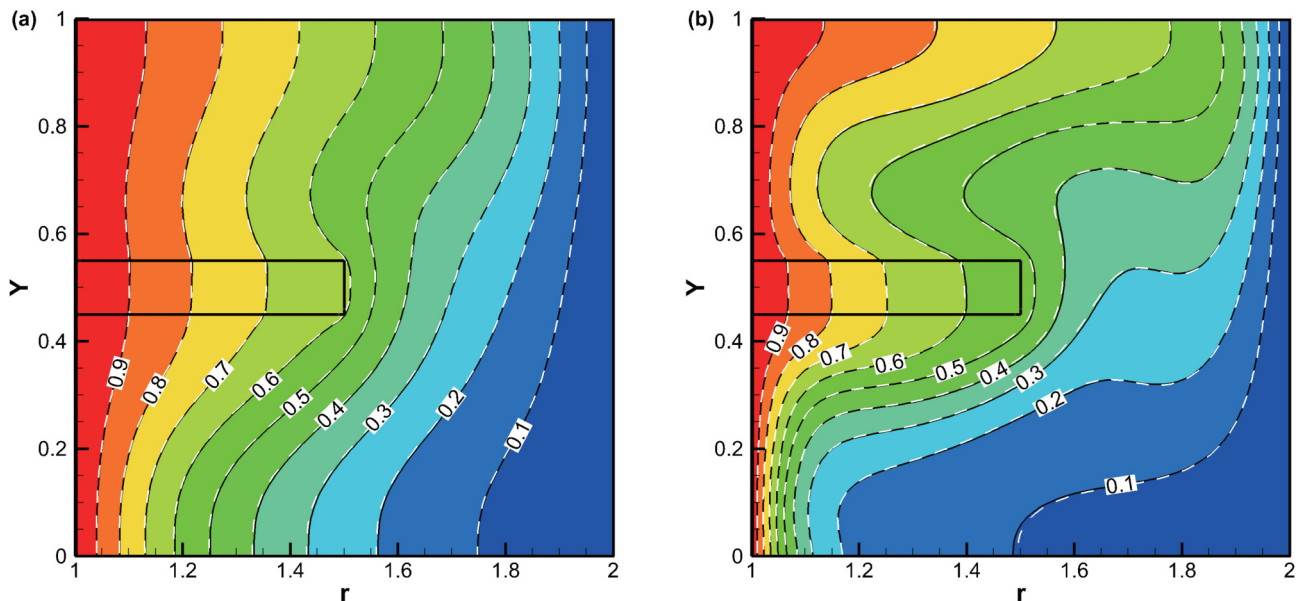


FIG. 12. Comparison of temperature contours at $z = 0$ plane for steady natural convection in a finned 3D annulus at (a) $Ra = 10^4$ and (b) $Ra = 10^5$. (Present: colored background with black solid line; FLUENT: white dashed line.)

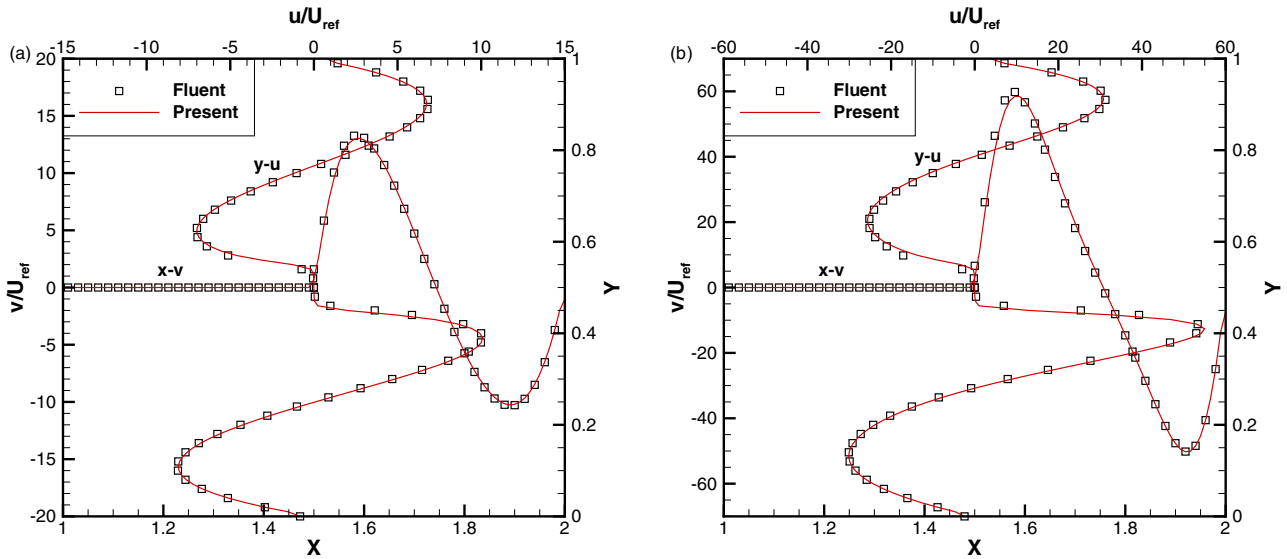


FIG. 13. Comparisons of u velocity profile along the vertical centerline and v velocity profile along the horizontal centerline at $z = 0$ plane for steady natural convection in a finned 3D annulus at (a) $Ra = 10^4$ and (b) $Ra = 10^5$.

easily. As a result, more significant convection heat transfer in this area is achieved for the natural convection in a finned 3D annulus. The average Nusselt numbers on the inner cylindrical surface are tabulated in Table III and compared with the results of FLUENT. Once again, the present results agree well with the reference data, which demonstrates the accuracy and effectiveness of the present solver for simulation of steady fluid-solid conjugate heat transfer problems on nonuniform mesh and curved boundaries.

In addition, the unsteady fluid-solid conjugate heat transfer problem in a finned 3D annulus is simulated. Like the unsteady natural convection in a finned 3D cavity, the ratio of specific heat is taken as $R_C = 20$, the initial temperature is set as $(T_0 + T_1)/2$, and the initial velocity is specified as 0. The computed temperature profile along the horizontal centerline on the $z = 0$ plane and u velocity profile along the vertical

centerline on the $z = 0$ plane at time $t = 0.01, 0.02$, and 0.05 s are shown in Figs. 14 and 15, respectively. Also included in these figures are the results obtained by FLUENT. Obviously, the quantitative results obtained from the present solver agree well with the reference solutions. Moreover, for the case of $Ra = 10^4$, the peak velocity increases monotonically with time, while for the case of $Ra = 10^5$, the peak velocity first increases and then decreases. This phenomenon is the same as that of the unsteady natural convection in a finned 3D cavity.

V. CONCLUSIONS

This work presents a 3D LBFS for simulation of fluid-solid conjugate heat transfer problems with a curved boundary. To accurately recover the energy equation of conjugate heat

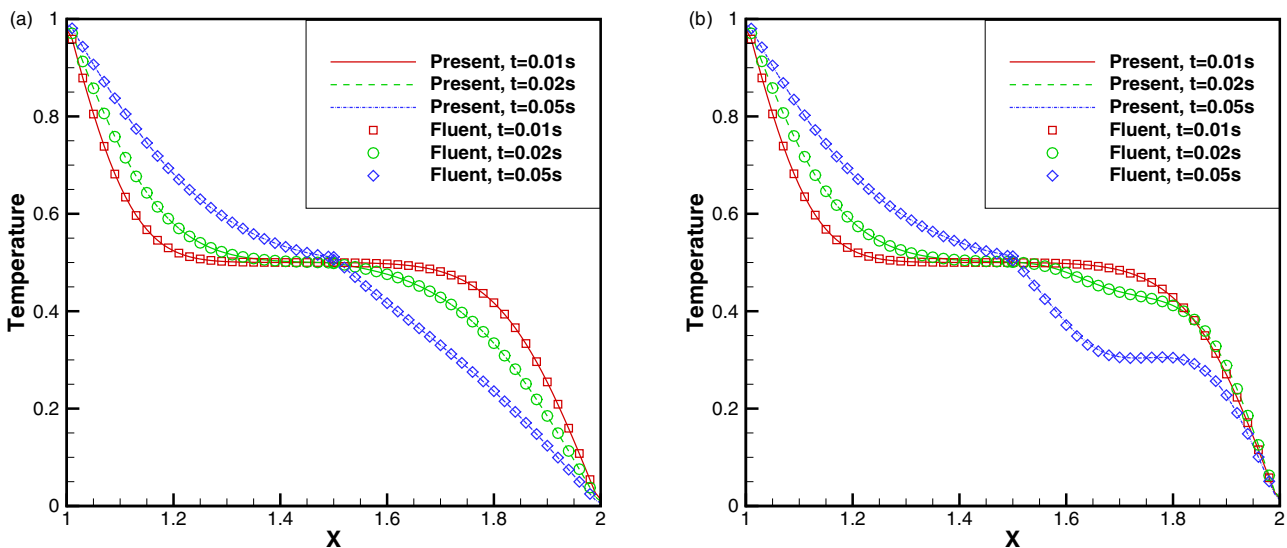


FIG. 14. Comparison of temperature profile along the horizontal centerline at $z = 0$ plane for unsteady natural convection in a finned 3D annulus at (a) $Ra = 10^4$ and (b) $Ra = 10^5$.

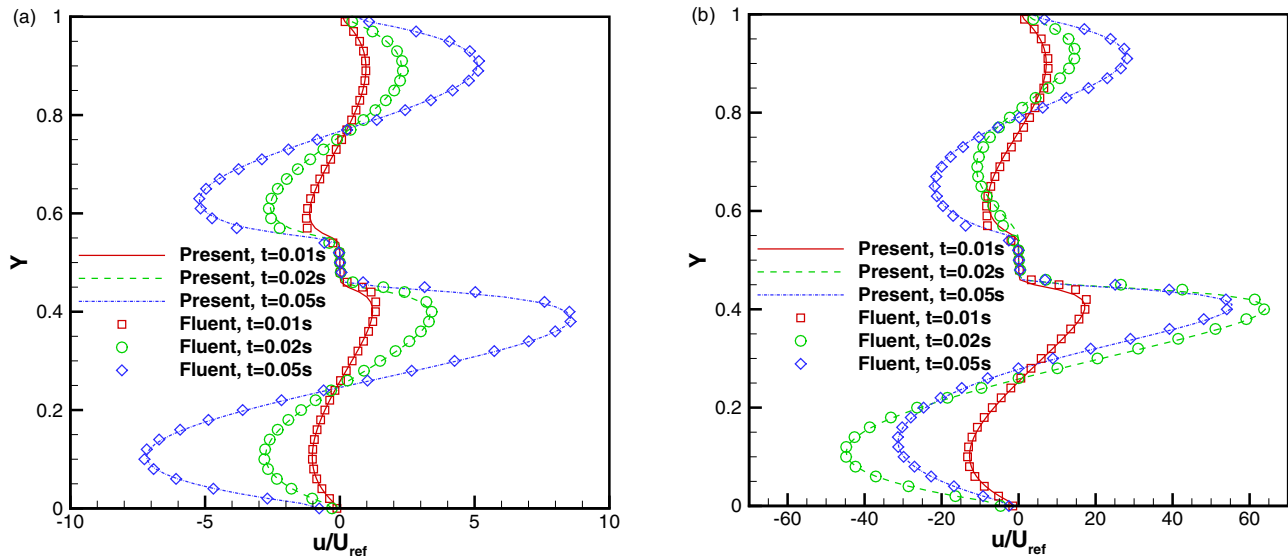


FIG. 15. Comparison of u velocity profile along the vertical centerline at $z = 0$ plane for unsteady natural convection in a finned 3D annulus at (a) $Ra = 10^4$ and (b) $Ra = 10^5$.

transfer problems, the total enthalpy distribution function (D3Q7 model) is chosen to reconstruct the numerical flux of the energy equation. For calculation of the numerical fluxes of continuity and momentum equations, the density distribution function (D3Q15 model) is adopted. Through the Chapman-Enskog expansion analysis, it is found that the distribution function truncated to the Navier-Stokes level is actually the function of equilibrium states at the cell interface and its surrounding points, which can be computed easily by the interpolation technique. As a result, the macroscopic fluxes at the cell interface can be calculated by the moments of these particle distribution functions.

The steady and unsteady natural convection in a finned 3D cavity and in a finned 3D annulus are simulated to validate the performance of the present solver. Numerical results

are compared well with the reference data and the results of FLUENT. These test cases demonstrate the accuracy and flexibility of the present solver for simulation of 3D fluid-solid conjugate heat transfer problems on a nonuniform mesh and curved boundary. For simulation of unsteady flows, it is shown that the computational efficiency of the present solver is comparable with that of FLUENT. Thus, it is believed that the present method has great potential for solving the problems of conjugate heat and mass transfer in practice.

ACKNOWLEDGMENT

This research is supported by the National Natural Science Foundation of China (Grants No. 11772157 and No. 11832012).

- [1] M. M. Mohamed, Air cooling characteristics of a uniform square modules array for electronic device heat sink, *Appl. Therm. Eng.* **26**, 486 (2006).
- [2] X. Wei, Y. Joshi, and M. K. Patterson, Experimental and numerical study of a stacked microchannel heat sink for liquid cooling of microelectronic devices, *J. Heat Transfer* **129**, 1432 (2007).
- [3] Y. P. Cheng, T. S. Lee, and H. T. Low, Numerical simulation of conjugate heat transfer in electronic cooling and analysis based on field synergy principle, *Appl. Therm. Eng.* **28**, 1826 (2008).
- [4] A. Ben-Nakhi and M. A. Mahmoud, Conjugate turbulent natural convection in the roof enclosure of a heavy construction building during winter, *Appl. Therm. Eng.* **28**, 1522 (2008).
- [5] M. A. Antar and H. Baig, Conjugate conduction-natural convection heat transfer in a hollow building block, *Appl. Therm. Eng.* **29**, 3716 (2009).
- [6] M. A. Antar, Thermal radiation role in conjugate heat transfer across a multiple-cavity building block, *Energy* **35**, 3508 (2010).
- [7] Q. Kang, D. Zhang, P. C. Lichtner, and I. N. Tsimpanogiannis, Lattice Boltzmann model for crystal growth from supersaturated solution, *Geophys. Res. Lett.* **31**, L21604 (2004).
- [8] O. V. Smirnova and V. V. Kalaev, 3D unsteady numerical analysis of conjugate heat transport and turbulent/laminar flows in LEC growth of GaAs crystals, *Int. J. Heat Mass Transf.* **47**, 363 (2004).
- [9] B. A. Y. Zvirin, A novel algorithm to investigate conjugate heat transfer in transparent insulation: Application to solar collectors, *Numer. Heat Transfer, Part A* **35**, 757 (1999).
- [10] S. Du, M. J. Li, Q. Ren, Q. Liang, and Y. L. He, Pore-scale numerical simulation of fully coupled heat transfer process in porous volumetric solar receiver, *Energy* **140**, 1267 (2017).
- [11] S. Chen and G. D. Doolen, Lattice Boltzmann method for fluid flows, *Annu. Rev. Fluid Mech.* **30**, 329 (1998).
- [12] C. K. Aidun and J. R. Clausen, Lattice-Boltzmann method for complex flows, *Annu. Rev. Fluid Mech.* **42**, 439 (2010).

- [13] S. Succi, *The Lattice Boltzmann Equation: For Fluid Dynamics and Beyond* (Oxford University Press, Oxford, England, 2001).
- [14] Z. Guo and C. Shu, *Lattice Boltzmann Method and its Applications in Engineering* (World Scientific, Singapore, 2013).
- [15] J. Wang, M. Wang, and Z. Li, A Lattice Boltzmann algorithm for fluid-solid conjugate heat transfer, *Int. J. Therm. Sci.* **46**, 228 (2007).
- [16] M. Wang and N. Pan, Modeling and prediction of the effective thermal conductivity of random open-cell porous foams, *Int. J. Heat Mass Transfer* **51**, 1325 (2008).
- [17] A. Tarokh, A. A. Mohamad, and L. Jiang, Simulation of conjugate heat transfer using the Lattice Boltzmann method, *Numer. Heat Trans., A* **63**, 159 (2013).
- [18] F. Meng, M. Wang, and Z. Li, Lattice Boltzmann simulations of conjugate heat transfer in high-frequency oscillating flows, *Int. J. Heat Fluid Flow* **29**, 1203 (2008).
- [19] G. Imani, M. Maerefat, and K. Hooman, Lattice Boltzmann simulation of conjugate heat transfer from multiple heated obstacles mounted in a walled parallel plate channel, *Numer. Heat Trans. A* **62**, 798 (2012).
- [20] L. Li, C. Chen, R. Mei, and J. F. Klausner, Conjugate heat and mass transfer in the Lattice Boltzmann equation method, *Phys. Rev. E* **89**, 043308 (2014).
- [21] K. Guo, L. Li, G. Xiao, N. AuYeung, and R. Mei, Lattice Boltzmann method for conjugate heat and mass transfer with interfacial jump conditions, *Int. J. Heat Mass Transf.* **88**, 306 (2015).
- [22] Z. Hu, J. Huang, and W. A. Yong, Lattice Boltzmann method for convection-diffusion equations with general interfacial conditions, *Phys. Rev. E* **93**, 043320 (2016).
- [23] Y. T. Mu, Z. L. Gu, P. He, and W. Q. Tao, Lattice Boltzmann method for conjugated heat and mass transfer with general interfacial conditions, *Phys. Rev. E* **98**, 043309 (2018).
- [24] H. Karani and C. Huber, Lattice Boltzmann formulation for conjugate heat transfer in heterogeneous media, *Phys. Rev. E* **91**, 023304 (2015).
- [25] H. Rihab, N. Moudhaffar, B. N. Sassi, and P. Patrick, Enthalpic Lattice Boltzmann formulation for unsteady heat conduction in heterogeneous media, *Int. J. Heat Mass Transfer* **100**, 728 (2016).
- [26] S. Chen, Y. Y. Yan, and W. Gong, A simple Lattice Boltzmann model for conjugate heat transfer research, *Int. J. Heat Mass Transfer* **107**, 862 (2017).
- [27] M. Nouri, R. Hamila, S. Ben Nasrallah, and P. Perré, A three-dimensional enthalpic Lattice Boltzmann formulation for convection-diffusion heat transfer problems in heterogeneous media, *Numer. Heat Trans A* **72**, 330 (2017).
- [28] Y. Peng, C. Shu, and Y. T. Chew, Simplified thermal Lattice Boltzmann model for incompressible thermal flows, *Phys. Rev. E* **68**, 026701 (2003).
- [29] H. Yoshida and M. Nagaoka, Multiple-relaxation-time Lattice Boltzmann model for the convection and anisotropic diffusion equation, *J. Comput. Phys.* **229**, 7774 (2010).
- [30] Q. Li, K. H. Luo, Q. J. Kang, Y. L. He, Q. Chen, and Q. Liu, Lattice Boltzmann methods for multiphase flow and phase-change heat transfer, *Prog. Energy Combust. Sci.* **52**, 62 (2016).
- [31] R. Huang and H. Wu, Phase interface effects in the total enthalpy-based Lattice Boltzmann model for solid-liquid phase change, *J. Comput. Phys.* **294**, 346 (2015).
- [32] S. Chen, B. Yang, and C. Zheng, A Lattice Boltzmann model for heat transfer in heterogeneous media, *Int. J. Heat Mass Transfer* **102**, 637 (2016).
- [33] J. H. Lu, H. Y. Lei, and C. S. Dai, A unified thermal Lattice Boltzmann equation for conjugate heat transfer problem, *Int. J. Heat Mass Transfer* **126**, 1275 (2018).
- [34] D. Gao, Z. Chen, L. Chen, and D. Zhang, A modified Lattice Boltzmann model for conjugate heat transfer in porous media, *Int. J. Heat Mass Transfer* **105**, 673 (2017).
- [35] S. Chen, Simulation of conjugate heat transfer between fluid-saturated porous media and solid wall, *Int. J. Therm. Sci.* **124**, 477 (2018).
- [36] D. Li, Z. X. Tong, Q. Ren, Y. L. He, and W. Q. Tao, Three-dimensional Lattice Boltzmann models for solid-liquid phase change, *Int. J. Heat Mass Transfer* **115**, 1334 (2017).
- [37] J. H. Lu, H. Y. Lei, and C. S. Dai, An optimal two-relaxation-time Lattice Boltzmann equation for solid-liquid phase change: The elimination of unphysical numerical diffusion, *Int. J. Therm. Sci.* **135**, 17 (2019).
- [38] S. A. Hosseini, N. Darabiha, and D. Thévenin, Lattice Boltzmann advection-diffusion model for conjugate heat transfer in heterogeneous media, *Int. J. Heat Mass Transfer* **132**, 906 (2019).
- [39] C. Shu, Y. Wang, C. J. Teo, and J. Wu, Development of Lattice Boltzmann flux solver for simulation of incompressible flows, *Adv. Appl. Math. Mech.* **6**, 436 (2014).
- [40] Y. Wang, L. M. Yang, and C. Shu, From Lattice Boltzmann method to Lattice Boltzmann flux solver, *Entropy* **17**, 7713 (2015).
- [41] Y. Wang, C. Shu, and L. M. Yang, An improved multiphase Lattice Boltzmann flux solver for three-dimensional flows with large density ratio and high Reynolds number, *J. Comput. Phys.* **302**, 41 (2015).
- [42] Y. Cao and Y. Zhang, Investigation on the natural convection in horizontal concentric annulus using the variable property-based Lattice Boltzmann flux solver, *Int. J. Heat Mass Transfer* **111**, 1260 (2017).
- [43] L. M. Yang, C. Shu, W. M. Yang, and J. Wu, Simulation of conjugate heat transfer problems by Lattice Boltzmann flux solver, *Int. J. Heat Mass Transfer* **137**, 895 (2019).
- [44] L. M. Yang, C. Shu, W. M. Yang, and J. Wu, A simple gas kinetic scheme for simulation of 3D incompressible thermal flows, *Numer. Heat Trans., B* **72**, 450 (2017).
- [45] R. L. Frederick and S. G. Moraga, Three-dimensional natural convection in finned cubical enclosures, *Int. J. Heat Fluid Flow* **28**, 289 (2007).
- [46] A. Purusothaman, A. Baïri, and N. Nithyadevi, 3D natural convection on a horizontal and vertical thermally active plate in a closed cubical cavity, *Int. J. Numer. Methods Heat Fluid Flow* **26**, 2528 (2016).
- [47] G. Imani, Three-dimensional Lattice Boltzmann simulation of steady and transient finned natural convection problems with evaluation of different forcing and conjugate heat transfer schemes, *Comput. Math. Appl.* **74**, 1362 (2017).
- [48] Y. Wang, C. Shu, C. J. Teo, and L. M. Yang, A fractional-step Lattice Boltzmann flux solver for axisymmetric thermal flows, *Numer. Heat Trans., B* **69**, 111 (2016).